Check for updates

Synthesis of g-C₃N₄ nanosheet modified SnO₂ composites with improved performance for ethanol gas sensing

Jianliang Cao, [ID] [a] Cong Qin,[a] Yan Wang, [ID] *[b] Huoli Zhang,[a] Bo Zhang,[c] Yuxiao Gong,[a] Xiaodong Wang,[c] Guang Sun,[c] Hari Bala[c] and Zhanying Zhang*[c]

The composites of SnO_2 have attracted much interest in the last few years due to their excellent sensing properties. A series of composites were prepared with two-dimensional (2D) g-C_3N_4 nanosheet modified SnO_2 by a simple hydrothermal method in this work. The as-prepared composites were characterized by the techniques of powder X-ray diffraction (XRD), thermogravimetric analysis (TG), scanning electron microscopy (SEM), transmission electron microscopy (TEM), energy dispersive X-ray spectroscopy (EDS), N_2 sorption and X-ray photoelectron spectroscopy (XPS). The gas sensing measurement results indicated that the sensor based on g-C_3N_4/SnO_2 composite showed high sensitivity and excellent selectivity for detection of ethanol vapor. At 500 ppm of ethanol vapor, the response value (R_a/R_g) of 5 wt% 2D g-C_3N_4 modified SnO_2 was 240 at 300 °C. Therefore, the g-C_3N_4/SnO_2 composites have a great potential ethanol gas sensing application.

1. Introduction

Gas sensors have wide applications in many fields, such as environmental protection, toxic gas detection, emission monitoring, chemical process control and so on.[1–8] For ethanol sensors, many metal-oxides have been investigated as semiconductor gas sensors in recent years, such as hollow ZnO microspheres,[9] lance-shaped CuO nanostructures,[10] Au-functional NiO nanoparticles,[11] Mn-doped Co_3O_4,[12] α-Fe_2O_3@graphene nanostructures,[13] WO_3 nanofibers,[14] CdO and MnO_2 thin films,[15] and noble metal decorated SnO_2.[16] Moreover, for gas sensing materials, the composites of SnO_2 exhibit excellent sensing properties such as high response, low-cost, fast response and recovery, which have attracted much interest in the past few years.[17–24]

However, among these sensors, the poor electrical characteristics prevent their direct applications. g-C_3N_4 is an organic and nontoxic semiconductor, which has attracted much attention, exhibiting excellent photoactivity, photocatalysis and electron transport.[25,26] For example, She *et al.*[27] have reported that the CeO_2 nanoparticles were dispersed on the surface of the g-C_3N_4 and the CeO_2/g-C_3N_4 composites showed high photocatalytic activity and stability in the environment applications.

Furthermore, Zhang *et al.*[28] investigated the MnO_2/g-C_3N_4 sandwich nanocomposite which showed satisfying performance on turn-on fluorescence response. Recently, Zeng *et al.*[29] prepared the α-Fe_2O_3/g-C_3N_4 composites which displayed distinguished cataluminescence properties in the process of detecting H_2S gas. These reports indicate that g-C_3N_4 had the ability to improve electrical characteristics of metal oxides.

In this work, the 2D g-C_3N_4 nanosheets (2D g-C_3N_4) were synthesized according to the previous literature report.[30] The 2D g-C_3N_4 modified SnO_2 composites were prepared with 2D g-C_3N_4, $SnCl_4 \cdot 5H_2O$ and $NH_3 \cdot H_2O$ as the precursor materials by the hydrothermal method. The as-prepared samples were characterized by XRD, TG, SEM, TEM, N_2 sorption and XPS. The sensing properties of the g-C_3N_4/SnO_2 composites to ethanol gas were investigated in detail. The results showed that the 2D g-C_3N_4 can effectively improved sensing properties of SnO_2 to ethanol gas. The composite of 5 wt% 2D g-C_3N_4 modified SnO_2 has the optimum performance for detection of ethanol vapor.

2. Experimental

2.1 Chemicals

Urea, tin(IV) chloride pentahydrate ($SnCl_4 \cdot 5H_2O$) and ammonia water ($NH_3 \cdot H_2O$) were purchased from Sinopharm Chemical Reagent Co., Ltd. All reagents were of analytical grade without further purification.

2.2 Preparation of g-C₃N₄/SnO₂ composites

Graphitic carbon nitride (g-C_3N_4) was synthesized by the pyrolysis of urea in the muffle furnace, 20 g urea was put into an

[a]College of Chemistry and Chemical Engineering, Henan Polytechnic University, Jiaozuo 454000, PR China

[b]School of Safety Science and Engineering, State Key Laboratory Cultivation Base for Gas Geology and Gas Control, Henan Polytechnic University, Jiaozuo 454000, PR China. E-mail: yanwang@hpu.edu.cn; Fax: +86 391 3987440; Tel: +86 391 3987440

[c]School of Materials Science and Engineering, Henan Polytechnic University, Jiaozuo 454000, PR China. E-mail: zhangzy@hpu.edu.cn

alumina crucible with a cover, then heated to 250 °C within 110 min and kept at 250 °C for 1 h. The further treatment was performed at 350 and 550 °C for 2 h, respectively. The heating rate of the whole reaction was 2 °C min^{-1}. The yellow powder (g-C_3N_4) was collected. Typically, 5 wt% 2D g-C_3N_4 modified SnO_2 (g-C_3N_4-5P/SnO_2) was prepared with the following method. 0.1 g of 2D g-C_3N_4 was dispersed in 130 mL DI water with ultrasonic treatment for 4 h, and 4.65 g $SnCl_4 \cdot 5H_2O$ was added into 144 mL ethanol. Then, the $SnCl_4 \cdot 5H_2O$ ethanol solution was slowly added into the g-C_3N_4 solution with magnetic stirring. Subsequently, 14 mL $NH_3 \cdot H_2O$ was injected into the mixture solution. Finally, the mixture was transferred into a 500 mL Teflon-lined steel autoclave and the sealed tank was put into an oven and heated at 150 °C for 24 h. The resulting product was separated by centrifuging and washed several times with DI water and ethanol. Then, the product was dried at 60 °C for 12 h to obtain the composite. According to this method, the g-C_3N_4/SnO_2 composites with 2.5 wt% and 7.5 wt% g-C_3N_4 modified SnO_2 were also prepared and marked as g-C_3N_4-2.5P/SnO_2 and g-C_3N_4-7.5P/SnO_2. For the comparison purpose, the pure SnO_2 particles were prepared without adding 2D g-C_3N_4.

2.3 Characterization

X-ray diffraction (XRD) analysis was performed on a Bruker-AXS D8 Advance diffractometer, with CuK_α radiation at 40 kV and 25 mA in a scanning range of 10–80° (2θ). Thermogravimetry analysis (TG) was done on a NETZSCH STA449C Simultaneous Thermal Analyzer. Scanning electron microscope (SEM) images were performed on a FEI Quanta 250 FEG scanning electron microscope with an accelerating voltage of 30 kV. Transmission electron microscopy (TEM) analysis was performed on a JEOL JEM-2100 microscope, operating at 200 kV. The samples were dispersed in ethanol and treated with ultrasound for 5 min, and then deposited on a copper grid coated with preformed holey carbon film. N_2 adsorption–desorption isotherms were collected at liquid nitrogen temperature using a Quantachrome Autosorb-iQ sorption analyzer, and the sample was degassed at 150 °C for more than 6 h. The specific surface areas (S_{BET}) of the samples were calculated following the multi-point BET (Brunauer–Emmett–Teller) procedure. The pore size distributions were determined from the adsorption branch of the isotherms using the DFT method. X-ray photoelectron spectroscopy (XPS) measurements were carried out on a Perkin-Elmer PHI 5600 spectrophotometer with the MgK_α radiation, and the C 1s peak was fixed at a binding energy of 284.6 eV.

2.4 Fabrication and analysis of gas sensor

The gas-sensing properties were investigated by using an intelligent gas sensing analysis system of CGS-4TPS from Beijing Elite Tech Co., Ltd. The as-prepared sample was mixed with several drops of distilled water to form a paste. The paste was then coated onto a ceramic substrate (13.4 mm × 7 mm, screen-printed with Ag–Pd comb-like electrodes) to obtain the resistance-type sensor. The schematic diagram of the typical gas sensor and the measuring principle were shown in Fig. 1. The test gases were injected into the closed chamber (with a volume
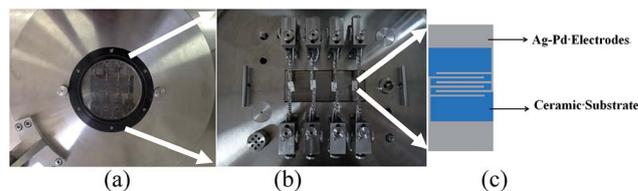

Fig. 1 (a) The appearance of the CGS-4TPS gas sensing test system, (b) the internal structure diagram of the test system, and (c) the structure diagram of the gas sensor substrate.

of 0.018 m^3) by a microinjector. In order to improve the stability and repeatability, the sensor was aged at 200 °C for 12 h. During the test, the operating temperature range was set at 200–380 °C, and the relative humidity was 40% in the test chamber. The gas response (S) was defined as the ratio of R_a/R_g, where R_a and R_g were the resistances of sensor measured in air and in test gas, respectively. The response and recovery times were defined as the time required for a change in response reach 90% of the equilibrium value after injecting and removing the test gas.

3. Results and discussion

3.1 Characterization of 2D g-C_3N_4, SnO_2 and g-C_3N_4/SnO_2 composites

XRD patterns of the as-prepared samples are displayed in Fig. 2. As can be seen from Fig. 2(a), two diffraction peaks at 13.1° and 27.5° can be observed, which were accorded to the (100) and (002) plane of g-C_3N_4. These two peaks could be due to the inter-layer structure of tri-*s*-triazine unit with interplanar spacing and the conjugated aromatic system, respectively,[29] which indicated that g-C_3N_4 was prepared successfully. Fig. 2(c–e) shows the XRD patterns of g-C_3N_4/SnO_2 composites with different content of g-C_3N_4. It can be observed obviously that some diffraction peaks are seen at 2 theta of 26.61°, 33.89°, 37.94°, 51.78°, 65.93°, which are assigned to the (110), (101), (200), (211) and (301) planes of the tetragonal rutile structure SnO_2 (JCPDS card no. 41-1445), respectively. However, compared with the XRD pattern
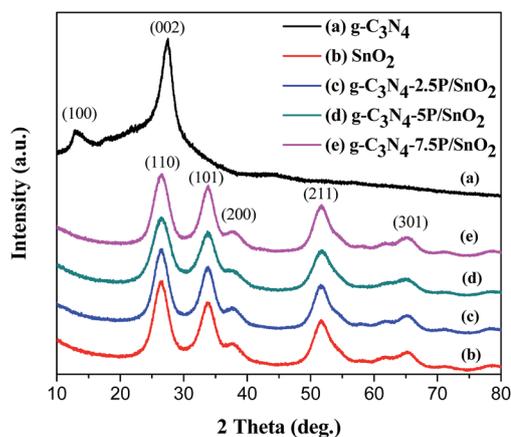

Fig. 2 XRD patterns of (a) 2D g-C_3N_4, (b) SnO_2, (c) g-C_3N_4-2.5P/SnO_2, (d) g-C_3N_4-5P/SnO_2 and (e) g-C_3N_4-7.5P/SnO_2.

of pure SnO_2 in Fig. 2(b), no diffraction peaks of g-C_3N_4 can be observed in the patterns of g-C_3N_4/SnO_2 composites. The main reason is the relatively low g-C_3N_4 content. Meanwhile, the diffraction peak of g-C_3N_4 at 27.5° could probably be overlapped with the strong diffraction peak of SnO_2 at 26.6°.

TG analysis was carried out from 20 to 700 °C with a heating rate of 10 °C min^{-1} under air atmosphere to reveal the thermal stability of g-C_3N_4, g-C_3N_4-2.5P/SnO_2, g-C_3N_4-5P/SnO_2 and g-C_3N_4-7.5P/SnO_2 at different temperatures. As is shown in Fig. 3, in the range of 50–150 °C of the curves, moisture and impurities were lost a little part weight. The second agravity peak is between 150 and 350 °C, which is due to the desorption of solvent. With increase of the temperature, a fast weight loss attributed to the decomposition of g-C_3N_4 was observed in the range of 450–620 °C. As shown in the profile of g-C_3N_4-5P/SnO_2, the remanent content of the composite is 83% after the decomposition of g-C_3N_4. It is demonstrated that g-C_3N_4 has good thermal stability and can be used to modify the sensing materials when the operating temperature is below 400 °C and the g-C_3N_4 is not decomposed in the process of the gas sensing tests.

As is shown in Fig. 4(a), the morphologies of the as-prepared g-C_3N_4 possess many wrinkles with overlap at the edges, which demonstrates that it possesses the two dimensional (2D) nanolamellar structure. From Fig. 4(b), we can find many irregular SnO_2 particles with different sizes. The result in Fig. 4(c) indicates that some SnO_2 particles are dispersed on the surface of 2D g-C_3N_4 nanosheets. It shows that it is a suitable route to

synthesize g-C_3N_4/SnO_2 composites using the hydrothermal treatment. Fig. 5(a) shows a typical EDS spectrum of g-C_3N_4-5P/SnO_2 composite. It is noted that four elements of Sn, O, C and N are synchronous existent in the same area observed in Fig. 5(b–f). The percentage composition of the four elements of C, N, Sn and O are 5.25 wt%, 8.87 wt%, 56.0 wt% and 29.9 wt%, respectively. The EDS mapping of C, N, O and Sn elements corresponding to Fig. 5(b) are displayed in Fig. 5(c), (d), (e) and (f), respectively. According to Fig. 5, the structural feature of g-C_3N_4-5P/SnO_2 composite is that 2D g-C_3N_4 and SnO_2 particles are combined together effectively.

Furthermore, the 2D g-C_3N_4 and g-C_3N_4-5P/SnO_2 composite were characterized by TEM. As shown in Fig. 6(a), the pure g-C_3N_4 is two dimensional nanosheets with many wrinkles. Fig. 6(b) displays that the SnO_2 nanoparticles are highly distributed on the surface of the 2D g-C_3N_4. Fig. 6(c) shows the HRTEM image of g-C_3N_4-5P/SnO_2 composite, it can be seen that the SnO_2 nanoparticles with diameters of 3–5 nm.

The porosity of the g-C_3N_4-2.5P/SnO_2, g-C_3N_4-5P/SnO_2 and g-C_3N_4-7.5P/SnO_2 composites were verified by N_2-sorption analysis. Fig. 7 depicts N_2 adsorption–desorption isotherm and the corresponding pore size distribution of the composites. The isotherms (Fig. 7(a)) of the samples are of classical type IV, which possess the characteristic of mesoporous materials according to the IUPAC. The hysteresis loop in the range of 0.4–1.0 (P/P_0) belong to the H3-type, which indicates the presence of mesoporous structure in the composites.[30] The pore size distribution curves of the g-C_3N_4-2.5P/SnO_2, g-C_3N_4-5P/SnO_2
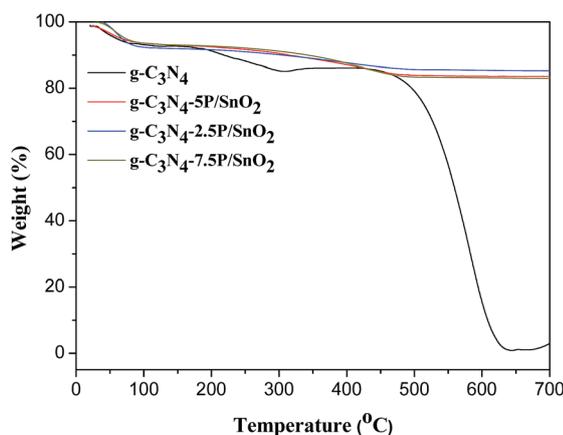

Fig. 3 TG profiles of 2D g-C_3N_4, g-C_3N_4-2.5P/SnO_2, g-C_3N_4-5P/SnO_2 and g-C_3N_4-7.5P/SnO_2 composites.
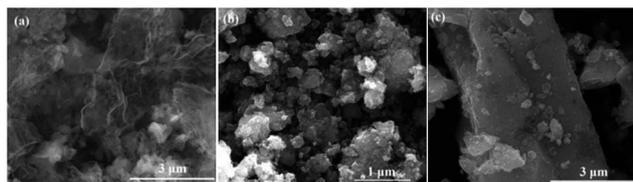
Fig. 4 SEM images of (a) 2D g-C_3N_4, (b) SnO_2 particles, and (c) g-C_3N_4-5P/SnO_2 composite.
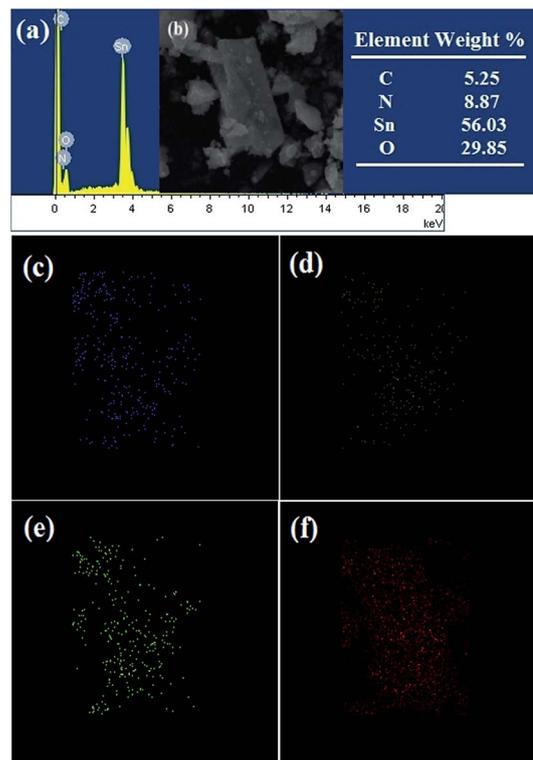

Fig. 5 (a) EDS spectra of the g-C_3N_4-5P/SnO_2 composite, (b) SEM image and elements content for selected EDS area, and EDS mappings of C (c), N (d), O (e), Sn (f) element related to (b).
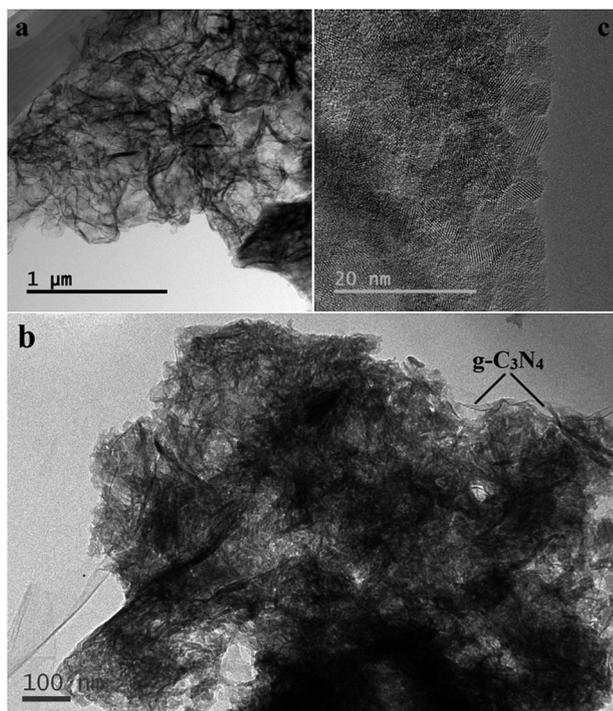
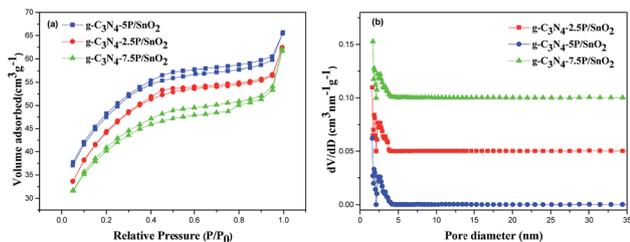**Fig. 6** TEM images of (a) 2D g-C_3N_4, (b) g-C_3N_4-5P/SnO_2 composite, and (c) HRTEM image of the g-C_3N_4-5P/SnO_2 composite.

Fig. 7 (a) N_2 adsorption–desorption isotherms and (b) the pore size distribution curves of the g-C_3N_4-2.5P/SnO_2, g-C_3N_4-5P/SnO_2 and g-C_3N_4-7.5P/SnO_2 composites. The volume adsorbed value was shifted by 3 units for the curve of data set g-C_3N_4-2.5P/SnO_2; The dV/dD values were shifted by 0.05 and 0.1 units for the curves of data sets g-C_3N_4-2.5P/SnO_2 and g-C_3N_4-7.5P/SnO_2, respectively.

and g-C_3N_4-7.5P/SnO_2 composites are shown in Fig. 7(b). The curves depict that the samples have relatively small pores with a size distribution of 1–5 nm and the pores are concentrated upon 2.6 nm according to the DFT method. The specific surface area of g-C_3N_4-2.5P/SnO_2, g-C_3N_4-5P/SnO_2 and g-C_3N_4-7.5P/SnO_2 composites are 117.6 m² g⁻¹, 160.2 m² g⁻¹ and 134.8 m² g⁻¹, respectively. The highest surface area of g-C_3N_4-5P/SnO_2 may make it possesses better gas sensing performance.

In order to investigate the heterojunction of the g-C_3N_4/SnO_2 composite, the XPS technique was carried out to obtain the interactions between SnO_2 and g-C_3N_4 (Fig. 8). Fig. 8(a) displays the survey scan spectra of g-C_3N_4, SnO_2 and g-C_3N_4-5P/SnO_2 composite. It is observed that Sn, O, C and N elements exist in the g-C_3N_4-5P/SnO_2 composite and Sn, O and C exist in SnO_2.

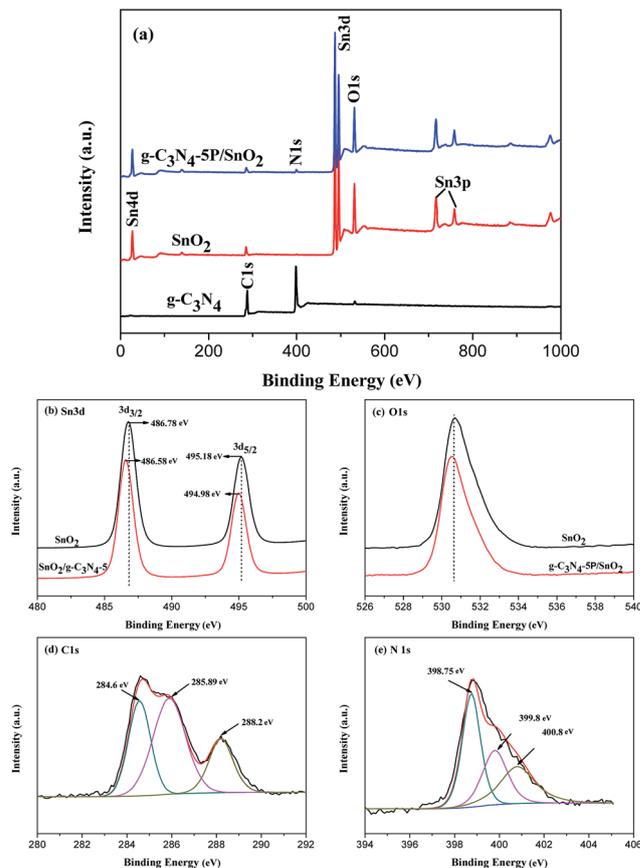**Fig. 8** XPS survey of g-C_3N_4, SnO_2 and g-C_3N_4-5P/SnO_2 samples: (a) the general scan spectrum, (b) Sn 3d spectrum, (c) O 1s spectrum, (d) C 1s spectrum, and (e) N 1s spectrum.

The C 1s peak from SnO_2 is due to the adventitious carbon. The XPS spectra of the g-C_3N_4 sample shows only C and N elements. As shown in Fig. 8(b), two signal peaks of Sn 3d in pure SnO_2 at binding energies of 486.78 eV and 495.18 eV are corresponding to Sn 3d$_{3/2}$ and Sn 3d$_{5/2}$, respectively. However, these two signal peaks of Sn 3d in g-C_3N_4-5P/SnO_2 had a shift. The peak positions are changed to 486.58 eV of Sn 3d$_{3/2}$ and 494.98 eV of Sn 3d$_{5/2}$, respectively. This phenomenon can be attributed to the interactions between g-C_3N_4 and Sn, and the heterojunction of interface region between g-C_3N_4 and SnO_2. For high resolution XPS spectra, as is shown in Fig. 8(c), there are few distinction of O 1s between SnO_2 and g-C_3N_4-5P/SnO_2. Fig. 8(d) displays the high resolution XPS spectra of C 1s. Three peaks for C 1s binding energies exist at 284.6 eV, 285.89 eV and 288.2 eV, respectively. As is well known, the signal at 284.6 eV corresponds to sp² C–C bonds, while the signal at 285.89 eV is identical to the combination of C–N groups. And the signal at 288.2 eV comes from the sp² C atoms from the aromatic rings N–C=N. It can be seen from Fig. 8(e) that there are three signals with binding energies at 398.75, 399.8 and 400.8 eV, respectively. The peak at 398.75 eV is ascribed to sp²-hybridized aromatic N bound to C atoms, the peak at 399.8 eV comes from the tertiary N bonded to C atoms in the form of N–(C)₃. And the peak at 400.8 eV is related to the N–H structure.

3.2 Gas-sensing properties

A series of gas-sensing tests were performed to investigate the properties of the $g-C_3N_4/SnO_2$ composites based sensors to ethanol vapor. For comparison, the pure SnO_2 based sensor was also tested. The operating temperature can strongly affect the chemical reaction happened on the surface of sensing materials. Herein, the response values (R_a/R_g) of the $g-C_3N_4/SnO_2$ composite and the pure SnO_2 based sensors to 500 ppm ethanol vapor were measured at different operating temperature. As can be seen from Fig. 9(a), all the sensors exhibited the similar variation tendency with the increase of operating temperature. And all the sensors reached the maximum response value at 300 °C due to the chemisorbed oxygen species achieving the required energy to react with ethanol vapor molecules. And the reaction effectively happened on metal oxides semiconductor surface varying the resistance significantly.[31] It can also be seen that the response values of the $g-C_3N_4/SnO_2$ composite based sensors are much higher than that of the pure SnO_2 based sensor. The response value of the composites increased with adding $g-C_3N_4$ content from 2.5 to 5 wt%. However, the response value decreased with the further increased $g-C_3N_4$ content. The response values of the pure SnO_2, $g-C_3N_4-2.5P/SnO_2$, $g-C_3N_4-5P/SnO_2$ and $g-C_3N_4-7.5P/SnO_2$ to 500 ppm ethanol are 180, 201, 240, and 210, respectively. A suitable content of $g-C_3N_4$ in the composite is beneficial to the dispersity and preferable heterojunctional structure, which can be formed in the interface region between 2D $g-C_3N_4$ and SnO_2. However, when the $g-C_3N_4$ content in the composites exceed a value (e.g. 5 wt% in this work), it may form the connection of bulk. As a result, the specific surface area of the composite decrease and there are reduced active sites for adsorption oxygen and ethanol gas, leading to the degradation of gas sensing properties. Consequently, the gas sensor performance increases at first and decreases when the $g-C_3N_4$ content in the composites increases.[32] The high content of 2D $g-C_3N_4$ may lead to the connection of the $g-C_3N_4$ nanosheets, which could form the micro electric bridges on the surface. The micro electric bridges may result in the semiconductor's resistance reduced. Therefore, the response value of the $g-C_3N_4-7.5P/SnO_2$ composite sensor to ethanol vapor decreased. Thus, the optimum operating temperature is at 300 °C and the optimum $g-C_3N_4$ content is 5 wt% 2D $g-C_3N_4$ modified SnO_2 composite. Therefore, all of
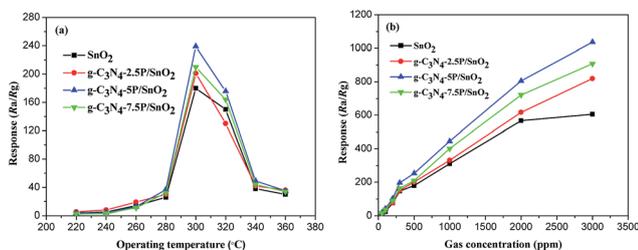
the further tests were carried on using the $g-C_3N_4-5P/SnO_2$ composite sensor at 300 °C. Fig. 9(b) shows the response values of all the sensors at different concentrations of ethanol at 300 °C. It can be seen that the response values increased promptly with the increasing of ethanol concentration in the range of 50–2000 ppm. However, the response values increased slowly when the ethanol concentration is in the range of 2000–3000 ppm. It can be concluded that the adsorption of these sensors to ethanol has reached approximately saturation. The response values of these sensors to ethanol at 300 °C from high to low are $g-C_3N_4-5P/SnO_2$, $g-C_3N_4-7.5P/SnO_2$, $g-C_3N_4-2.5P/SnO_2$ and SnO_2, respectively.

Fig. 10(a) displays the continuous response–recover curves of the pure SnO_2 and $g-C_3N_4-5P/SnO_2$ composite based sensors to different ethanol concentrations at 300 °C. Each response–recovery cycle was taken up about 500 s with a response interval of 250 s and a recovery interval of 250 s. It can be seen that the response values of the both sensors increased with the increase of ethanol concentration in the range of 50–5000 ppm. As seen in Fig. 10(a), the $g-C_3N_4-5P/SnO_2$ composite sensor exhibited much higher response value than that of pure SnO_2 sensor to ethanol vapor in the range of 50–5000 ppm. The response value of the $g-C_3N_4-5P/SnO_2$ composite sensor to 5000 ppm ethanol reached about 1900, which is nearly two times higher than that of the pure SnO_2 sensor. Response–recovery time is one of the most critical influential factor on the response of gas sensor. Fig. 10(b) shows the response–recovery time of the $g-C_3N_4-5P/SnO_2$ composite sensor to 2000 ppm ethanol at 300 °C. As seen in Fig. 10(b), the response promptly reached the maximum value when the $g-C_3N_4-5P/SnO_2$ composite sensor was exposed to ethanol vapor. And the response time and the recovery time are 15 s and 38 s, respectively.

The repeatability of sensing material plays an important role in the practical application of gas sensor. The repeatability of
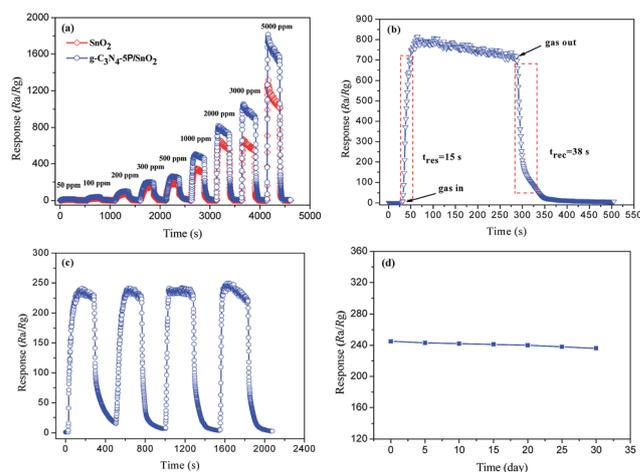
Fig. 10 (a) Real time response curves of the pure SnO_2 and $g-C_3N_4-5P/SnO_2$ composite sensors to ethanol in the range of 50–5000 ppm, (b) response–recovery time characteristics of the $g-C_3N_4-5P/SnO_2$ composite sensor to 2000 ppm ethanol at 300 °C, (c) repeatability and (d) stability behaviors of the $g-C_3N_4-5P/SnO_2$ composite sensor to 500 ppm ethanol at 300 °C.

Fig. 9 The response values of the SnO_2, $g-C_3N_4-2.5P/SnO_2$, $g-C_3N_4-5P/SnO_2$ and $g-C_3N_4-7.5P/SnO_2$ to 500 ppm ethanol (a) under different operating temperature, (b) for different concentrations of ethanol at 300 °C.

the g-C_3N_4-5P/SnO_2 composite based sensor to 500 ppm ethanol vapor was performed at 300 °C. Fig. 10(c) shows the response–recovery cycle curves. And the response values of the tests are 239, 241, 240 and 245, respectively. The g-C_3N_4-5P/SnO_2 composite sensor shows an excellent repeatable performance for ethanol gas sensing. Moreover, the stability of the g-C_3N_4-5P/SnO_2 composite based sensor was also investigated and a long-term response value was measured. Fig. 10(d) shows the response value of the g-C_3N_4-5P/SnO_2 composite based sensor was exposed to 500 ppm ethanol for 30 days. The response value was measured every 5 days and the response value was nearly kept at 240. It indicated that the g-C_3N_4-5P/SnO_2 composite sensor had a good stability, which could be one of the potential candidates for ethanol gas sensor. Selectivity is another pivotal criterion of gas sensor.

The selectivity of the pure SnO_2 and g-C_3N_4-5P/SnO_2 composite sensors to five different 500 ppm gases at 300 °C was investigated. The five different gases are respectively ethanol, methanol, formaldehyde, acetone and toluene. The response values were measured and the results are shown in Fig. 11. It is observed that the g-C_3N_4-5P/SnO_2 composite sensor has a better selectivity to ethanol than the pure SnO_2 sensor in the five different gases at 300 °C.

The performances of different sensing materials are listed in Table 1. As can be seen from Table 1, according to the literature, the response values of SnO_2@MoS_2,[22] ZnO/graphene,[8] In-doped SnO_2,[23] SnO_2/graphene[24] were 160, 280, 80, 38.58, respectively. In this work, the response value of 5 wt% 2D g-C_3N_4 modified SnO_2 to 500 ppm of ethanol vapor was 240 at 300 °C. Therefore, the g-C_3N_4/SnO_2 composites show the excellent sensing properties to ethanol vapor, which have a great potential application.

3.3 Gas sensing mechanism of the g-C_3N_4/SnO_2 composites

In general, for the g-C_3N_4/SnO_2 composites, the incorporation of 2D g-C_3N_4 plays an important role on preventing the aggregation of SnO_2 particles and forms a large surface area structure, which is beneficial to the adsorption and diffusion process of ethanol molecules. And the 2D g-C_3N_4 nanosheets can
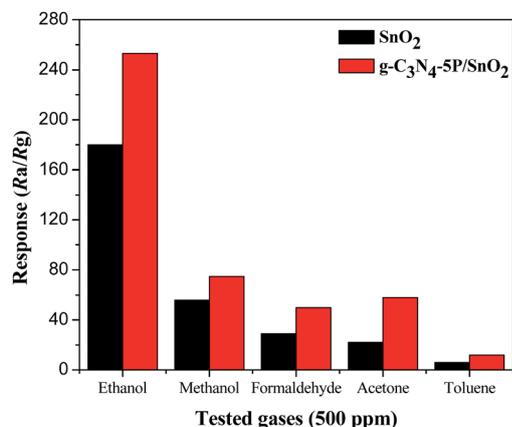
Table 1 The comparative analysis of the sensing performance between this work and previously reported results

Sensing materials	Ethanol concentration (ppm)	Temperature (°C)	Response (R_a/R_g)	Ref.
SnO_2@MoS_2	500	280	160	22
ZnO/graphene	500	400	280	8
In-doped SnO_2	500	300	80	23
SnO_2/graphene	600	27	38.58	24
SnO_2/g-C_3N_4	500	300	240	This work

provide more active sites to adsorb O_2 molecules and ethanol gas molecules. The improved gas sensing performance of the g-C_3N_4/SnO_2 composite sensor to ethanol could be mainly attributed to the heterojunction of interface region between g-C_3N_4 and SnO_2 and the interactions between Sn and g-C_3N_4. According to the XPS result, the shift of Sn 3d signal peaks illustrates that there are the interactions between Sn and g-C_3N_4. The electrical properties at the heterojunctions changes while ethanol gas molecules pass through the interface region between g-C_3N_4 and SnO_2. This coadjacent retiform structure could provide higher efficiency for the gas adsorption and diffusion between SnO_2 and g-C_3N_4. Both of SnO_2 and g-C_3N_4 are n-type semiconductor. The band gap are 3.71 eV and 2.7 eV, respectively. The conduction band level of g-C_3N_4 is negative than SnO_2. When SnO_2 and g-C_3N_4 were combined, they formed a heterojunction structure. The electrons will inflow from the conduction band of g-C_3N_4 to the conduction band of SnO_2, leading to a higher potential barrier. As a result, the electrons and holes are separated.[33] Meanwhile, the heterojunction structure may suppress the recombination of electron–hole and urge electrons to transfer quickly from ethanol vapour to the surface of SnO_2/g-C_3N_4. Therefore, this lead to a higher response because of the increased conductivity of the heterojunction structure.[32] In addition, surface adsorbed oxygen theory is also used to explain gas sensing mechanism. Oxygen molecules would adsorb on surface of SnO_2 and capture electrons from the conduction band of SnO_2 when the sensor was exposed in air (eqn (1)). Then oxygen molecules were ionized to O^{2-}, O^- and O_2^-, and the formation of depletion layers led to the increase of resistance of the composite sensor. Nevertheless, when the sensor was exposed into the ethanol gas, the ethanol molecules would react with oxygen ions absorbed on the surface of the sensor. As displayed in eqn (2) and (3), the ethanol molecules were oxidized into acetaldehyde and eventually turned into carbon dioxide and water. As a result, the trapped electrons released back to the depletion layer of the sensing film, resulting in the decrease of the resistance of the composite sensor.

$$O_2 + e^- \rightarrow O_2^- \quad (1)$$

$$2CH_3CH_2OH + O_2^- \rightarrow 2CH_3CHO + 2H_2O + e^- \quad (2)$$

$$2CH_3CHO + 5O_2^- \rightarrow 4CO_2 + 4H_2O + 5e^- \quad (3)$$

Fig. 11 Comparison of the response values of the pure SnO_2 and the g-C_3N_4-5P/SnO_2 composite sensors to 500 ppm different gases at 300 °C.

4. Conclusions

In summary, the g-C_3N_4/SnO_2 composites were prepared by a facile method through hydrothermal treatment. And it was found that the sensor based on g-C_3N_4/SnO_2 composite showed high sensitivity and excellent selectivity for detection of ethanol vapor. At 500 ppm of ethanol vapor, the response value (R_a/R_g) of 5 wt% 2D g-C_3N_4 modified SnO_2 was 240 at 300 °C. The improved sensing properties of the g-C_3N_4/SnO_2 composites are mainly attributed to the large specific surface and the modified electronic characteristics. Considering its facile effective synthesis approach, the g-C_3N_4/SnO_2 composite will be an ideal candidate for ethanol gas sensor application, optic devices and photocatalysis.

Acknowledgements

Notes and references

1 D. Zhang, J. Liu, H. Chang, A. Liu and B. Xia, Characterization of a hybrid composite of SnO_2 nanocrystal-decorated reduced graphene oxide for ppm-level ethanol gas sensing application, *RSC Adv.*, 2015, **5**, 18666–18672.

2 O. Korostynska, A. Mason, M. Ortoneda-Pedrolam and A. Al-Shamma'a, Electromagnetic wave sensing of NO_3 and COD concentrations for real-time environmental and industrial monitoring, *Sens. Actuators, B*, 2014, **198**, 49–54.

3 D. Zhang, J. Tong, B. Xia and Q. Xue, Ultrahigh performance humidity sensor based on layer-by-layer self-assembly of graphene oxide/polyelectrolyte nanocomposite film, *Sens. Actuators, B*, 2014, **203**, 263–270.

4 S. T. Navale, A. T. Mane, M. A. Chougule, N. M. Shinde, J. Kim and V. B. Patil, Highly selective and sensitive CdS thin film sensors for detection of NO_2 gas, *RSC Adv.*, 2014, **4**, 44547–44554.

5 H. Zhang, J. Feng, T. Fei, S. Liu and T. Zhang, SnO_2 nanoparticles-reduced graphene oxide nanocomposites for NO_2 sensing at low operating temperature, *Sens. Actuators, B*, 2014, **190**, 472–478.

6 N. Karmakar, R. Fernandes, S. Jain, U. V. Patil, N. G. Shimpi, N. V. Bhat and D. C. Kothari, Room temperature NO_2 gas sensing properties of *p*-toluenesulfonic acid doped silver-polypyrrole nanocomposite, *Sens. Actuators, B*, 2017, **242**, 118–126.

7 F. Perrozzi, S. M. Emamjomeh, V. Paolucci, G. Taglieri, L. Ottaviano and C. Cantalini, Thermal stability of WS_2 flakes and gas sensing properties of WS_2/WO_3 composite to H_2, NH_3 and NO_2, *Sens. Actuators, B*, 2017, **243**, 812–822.

8 S. Liang, J. Zhu, J. Ding, H. Bi, P. Yao, Q. Han and X. Wang, Deposition of cocoon-like ZnO on graphene sheets for improving gas-sensing properties to ethanol, *Appl. Surf. Sci.*, 2015, **357**, 1593–1600.

9 Y. Chen, X. Li, X. Li, J. Wang and Z. Tang, UV activated hollow ZnO microspheres for selective ethanol sensors at low temperatures, *Sens. Actuators, B*, 2016, **232**, 158–164.

10 A. Umar, J.-H. Lee, R. Kumar, O. Al-Dossary, A. A. Ibrahim and S. Baskoutas, Development of highly sensitive and selective ethanol sensor based on lance-shaped CuO nanostructures, *Mater. Des.*, 2016, **105**, 16–24.

11 S. Park, H. Kheel, G.-J. Sun, S. K. Hyun, S. E. Park and C. Lee, Ethanol sensing properties of Au-functional NiO nanoparticles, *Bull. Korean Chem. Soc.*, 2016, **37**, 713–719.

12 C. Stella, N. Soundararajan and K. Ramachandran, Undoped and Mn-doped Co_3O_4 nanorods for ethanol sensing, *J. Mater. Sci.: Mater. Electron.*, 2015, **26**, 4178–4184.

13 S. Liang, J. Zhu, C. Wang, S. Yu, H. Bi, X. Liu and X. Wang, Fabrication of α-Fe_2O_3@graphene nanostructures for enhanced gas-sensing property to ethanol, *Appl. Surf. Sci.*, 2014, **292**, 278–284.

14 S. Cao, C. Zhao, T. Han and L. Peng, Hydrothermal synthesis, characterization and gas sensing properties of the WO_3 nanofibers, *Mater. Lett.*, 2016, **169**, 17–20.

15 R. Chandiramouli and B. G. Jeyaprakash, Operating temperature dependent ethanol and formaldehyde detection of spray deposited mixed CdO and MnO_2 thin films, *RSC Adv.*, 2015, **5**, 43930–43940.

16 Y. V. Kaneti, J. Yue, J. Moriceau, C. Chen, M. Liu, Y. Yuan, X. Jiang and A. Yu, Experimental and theoretical studies on noble metal decorated tin oxide flower-like nanorods with high ethanol sensing performance, *Sens. Actuators, B*, 2015, **219**, 83–93.

17 V. Srivastava and K. Jain, At room temperature graphene/SnO_2 is better than MWCNT/SnO_2 as NO_2 gas sensor, *Mater. Lett.*, 2015, **169**, 28–32.

18 Z. Song, Z. Wei, B. Wang, Z. Luo, S. Xu, W. Zhang, H. Yu, M. Li, Z. Huang, J. Zang, F. Yi and H. Liu, Sensitive Room-Temperature H_2S Gas Sensors Employing SnO_2 Quantum Wire/Reduced Graphene Oxide Nanocomposites, *Chem. Mater.*, 2016, **28**, 1205–1212.

19 S. Mao, S. Cui, G. Lu, K. Yu, Z. Wen and J. Chen, Tuning gas-sensing properties of reduced graphene oxide using tin oxide nanocrystals, *J. Mater. Chem.*, 2012, **22**, 11009–11013.

20 S. Das and V. Jayaraman, SnO_2: A comprehensive review on structures and gas sensors, *Prog. Mater. Sci.*, 2014, **66**, 112–255.

21 M. Narjinary, P. Rana, A. Sen and M. Pal, Enhanced and selective acetone sensing properties of SnO_2-MWCNT nanocomposites: Promising materials for diabetes sensor, *Mater. Des.*, 2017, **115**, 158–164.

22 H. Yan, P. Song, S. Zhang, Z. Yang and Q. Wang, Dispersed SnO_2 nanoparticles on MoS_2 nanosheets for superior gas-sensing performances to ethanol, *RSC Adv.*, 2015, **5**, 79593–79599.

23 K. Inyawilert, A. Wisitsoraat, C. Sriprachaubwong, A. Tuantranont, S. Phanichphant and C. Liewhiran, Rapid ethanol sensor based on electrolytically-exfoliated graphene-loaded flame-made In-doped SnO_2 composite film, *Sens. Actuators, B*, 2015, **209**, 40–55.

24 M. T. V. O. Jayaweera, R. C. L. De Silva, I. R. M. Kottegoda and S. R. D. Rosa, Synthesis, characterization and ethanol vapor sensing performance of SnO_2/Graphene composite film, *J. Phys.*, 2015, **15**, 1–10.

25 H. Dai, S. Zhang, G. Xu, Y. Peng, L. Gong, X. Li, Y. Li, Y. Lin and G. Chen, Highly photoactive heterojunction based on g-C_3N_4 nanosheets decorated with dendritic zinc(II) phthalocyanine through axial coordination and its ultrasensitive enzyme-free sensing of choline, *RSC Adv.*, 2014, **4**, 58226–58230.

26 Q. Lu, J. Zhang, X. Liu, Y. Wu, R. Yuan and S. Chen, Enhanced electrochemiluminescence sensor for detecting dopamine based on gold nanoflower@graphitic carbon nitride polymer nanosheet-polyaniline hybrids, *Analyst*, 2014, **139**, 6556–6562.

27 X. She, H. Xu, H. Wang, J. Xia, Y. Song, J. Yan, Y. Xu, Q. Zhang, D. Du and H. Li, Controllable synthesis of CeO_2/ g-C_3N_4 composites and their applications in the environment, *Dalton Trans.*, 2015, **44**, 7021–7031.

28 X. L. Zhang, C. Zheng, S. S. Guo, J. Li, H. H. Yang and G. Chen, Turn-on fluorescence sensor for intracellular imaging of glutathione using g-C_3N_4 nanosheet-MnO_2 sandwich nanocomposite, *Anal. Chem.*, 2014, **86**, 3426–3434.

29 B. Zeng, L. Zhang, X. Wan, H. Song and Y. Lv, Fabrication of α-Fe_2O_3/g-C_3N_4 composites for cataluminescence sensing of H_2S, *Sens. Actuators, B*, 2015, **211**, 370–376.

30 J. L. Cao, Y. Wang, T. Y. Zhang, S. H. Wu and Z. Y. Yuan, Preparation, characterization and catalytic behavior of nanostructured mesoporous CuO/$Ce_{0.8}Zr_{0.2}O_2$ catalysts for low-temperature CO oxidation, *Appl. Catal., B*, 2008, **78**, 120–128.

31 Y. Xiao, Q. Yang, Z. Wang, R. Zhang, Y. Gao, P. Sun, Y. Sun and G. Lu, Improvement of NO_2 gas sensing performance based on discoid tin oxide modified by reduced graphene oxide, *Sens. Actuators, B*, 2016, **227**, 419–426.

32 Y. Zhang, D. Zhang, W. Guo and S. Chen, The α-Fe_2O_3/g-C_3N_4 heterostructural nanocomposites with enhanced ethanol gas sensing performance, *J. Alloys Compd.*, 2016, **685**, 84–90.

33 Y. Zang, L. Li, X. Li, R. Lin and G. Li, Synergistic collaboration of g-C_3N_4/SnO_2 composites for enhanced visible-light photocatalytic activity, *Chem. Eng. J.*, 2014, **246**(16), 277–286.